MOX–Report No. 27/2010

An adaptive algorithm for topology optimization with goal-oriented error control

Matteo Bruggi, Marco Verani

MOX, Dipartimento di Matematica "F. Brioschi"
Politecnico di Milano, Via Bonardi 9 - 20133 Milano (Italy)

mox@mate.polimi.it http://mox.polimi.it

An adaptive algorithm for topology optimization with goal-oriented error control

Matteo Bruggi[a] and Marco Verani[b]

25th, July 2010

[a] Department of Structural Mechanics,
Università di Pavia, Via Ferrata 1, I27100 Pavia, Italy.
matteo.bruggi@unipv.it

[b] MOX - Modelling and Scientific Computing, Department of Mathematics,
Politecnico di Milano, Via Bonardi 9, I20133 Milano, Italy
marco.verani@polimi.it

Abstract

We present an adaptive scheme, named ATOPT algorithm, to address volume–constrained compliance minimization, a benchmark problem in topology optimization. The algorithm performs a set of optimization loops on an underlying grid that is iteratively adapted to improve the description quality of the topology of the structure and the accuracy of the finite element compliance approximation of the evolving solution. Two suitable error estimators are defined in order to address both the issues. Numerical simulations show that ATOPT algorithm achieves optimal layouts that are in full agreement with standard results obtained by employing large scale uniformly refined grids. However, the ATOPT algorithm turns out to be more accurate in terms of the approximation of both the elastic behavior and the topology, while the computational cost spent in the minimization algorithm is remarkably reduced.

Keywords: topology optimization, minimum compliance, adaptive mesh refinement.
2000 Mathematics Subject Classification. 65N30, 93B40

1 Introduction

Topology optimization is a fertile area of research that is mainly concerned with the automatic generation of optimal layouts to solve design problems in engineering. The classical formulation addresses the need of finding the best distribution of isotropic material that minimizes the work of the external works at equilibrium, while respecting a constraint on the assigned amount of volume. This is the so–called minimum compliance formulation that was introduced a few decades ago by the pioneering work in [5].

The considered optimization framework is based on the adoption of a penalization of the elastic properties of the medium that depends on the local values of the density field. A classical material model is the well–known SIMP (Solid Isotropic Material with Penalization), see e.g. [5], [7] and [40], while other interpolations have been successively formulated to address more specific needs. This is the case of the RAMP (Rational Approximation of Material Properties) originally introduced by [35], which is especially conceived to cope with problems including self–weight [11] and multi–phase interpolations [33, 39]. The solution of the arising minimization problem may be tackled, among the others, by the optimality criteria, see e.g. [27], or resorting to the methods of mathematical programming which may be straightforwardly applied to general multi–constrained formulations. Two algorithms are extensively used in the literature for their many successes with several kind of objective functions and constraints in large scale problems, i.e. the Methods of Moving Asymptotes (MMA), by [37], and the optimizer CONLIN, by [16].

Topology optimization has nowadays a very wide area of applications that refer not only to the original structural problems, but also to many multidisciplinary fields of engineering, see also [6]. Reference is made to [26] and [30], for comprehensive reviews on the topic, and to [8], for theoretical and practical issues related to methods, algorithms and applications of the discipline.

A classical strategy for the solution of a topology optimization problem resorts to the discretization of the density field to tackle the minimization setting, along with the adoption of finite element methods to cope with the approximation of the relevant state equation. The same mesh is generally used to address the two discretizations.

Referring to minimum compliance problems, a standard approach implements low–order displacement–based finite elements that are coupled with an element–wise density discretization. Such a scheme is affected by numerical instabilities like checkerboard and mesh dependence. The arising of the first drawback depends on the choice of displacement shape function with respect to the adopted density approximation, while the second is the discrete counterpart of a well–known ill–posedness of the continuous topology optimization problem. Checkerboard and mesh dependence of the optimal solution may be easily solved via ad hoc filtering techniques that preserve the advantages of the above mentioned discrete approach, see e.g. [14, 34].

The outlined setting has a computational cost that straightforwardly depends on the refinement of the mesh. Large scale grids improve the accuracy of the topology description along with the approximation of its mechanical behavior, but involve an increased number of density and displacement unknowns. The first number affects the time spent within the optimizer, while the second controls the computational burden related to the call of the finite element solver. To release the cost of the optimization procedure without losing the benefits of large scale meshes, a few strategies have been originally investigated in the literature based on the adoption of multiple grids. The contribution in [21] introduces the idea of the iterative solution of the optimization problem to be performed on finer and finer uniform meshes. Each sub–optimal design is used as a starting point for the subsequent minimization, as also done in the two–stage approach

proposed by [23]. The works by [20] and [18] exploit the adoption of uniform grids with different size in order to cope with the enlarging and the possible adjusting of the design space. An adaptive refinement driven by the detection of the evolving solid-void interface is proposed in the contribution by [31], that exploits a multi–level approach based on a RAMP–based filtered scheme coupled to a linear material interpolation with penalty constraint. The work in [36] points out the advantage provided by coarsening operations within the cavities of the optimal design and also remarks the need for a suitable uniform refinement in and around the full material zones. This is addressed as an important issue to avoid wrong convergence in sub–optimal results that may be encountered in earlier coarse grids.
An alternative approach to the solution of the discrete topology problem on multiple size meshes consists in the adoption of two different discretizations for the approximation of the density field and the solution of the finite element equations. The method was originally introduced by the work in [24] that adopts smoothing algorithms to project the design unknowns on a mesh refined according to the material distribution in the design model. The same approach has also been extended in [25] to address a non–linear formulation for the topology optimization of elasto–plastic structures. An alternative version of this approach is followed by [12], while the recent contribution in [17] resorts to a separate design variable field to control the cardinality of the design space. In their works the authors implement a predefined analysis mesh, but they remark the importance to provide adaptive grids in order to improve the accuracy of the finite element approximation. They also present a detailed discussion on mesh dependence and checkerboard within the context of multilevel grids.
Regardless of the adoption of one or two approximations for the density field and the approximation of the elasticity equations, all the above contributions point out that the resort to multiple mesh computations may remarkably release the computational burden of standard methods. This is mainly done implementing different sizes of a uniform grid or introducing ad hoc refinement and de–refinement procedures. These strategies are generally driven by parameters that capture the change of the domain based on estimators of the evolution of the density distribution. A uniform refinement is hence provided to the 0–1 interface and, in certain cases, to the bulk of the full material design.
Within the above framework, this paper has the aim of proposing an alternative adaptive strategy, named `ATOPT` (Adaptive Topology Optimization) algorithm, to cope with volume–constrained compliance minimization. Our adaptive algorithm is an iterative scheme of the form

$$\texttt{OPTIMIZE} \rightarrow \texttt{ESTIMATE} \rightarrow \texttt{MARK} \rightarrow \texttt{REFINE} \rightarrow \texttt{COARSEN}$$

and it resorts to the adoption of the same mesh of triangular elements to address the element–wise constant discretization of the density field and to solve a finite element analysis based on linear displacement shape functions. This allows to exploit a very standard scheme for the solution of a set of minimization problems that are iteratively defined on the underlying adaptive grid. The minimization algorithm (implemented in the module `OPTIMIZE`) is set to work on filtered sensitivities, as a classical way to

avoid the above outlined numerical instabilities. The adaptive procedure is driven by two error estimators (computed in the module `ESTIMATE`), referring to the error in the description of the optimal topology (Topological Error) and to the error due to the finite element approximation of the compliance functional (Compliance Error), respectively. As a consequence, our algorithm provides an adaptive discretization that remarkably improves the topology description along with the approximation of its mechanical behavior. In particular, the error estimator for the compliance error hinges upon classical Dual Weighted Residual (DWR) method [4, 3], while the error indicator for the topological error is heuristic and it is presented in Section 3.5. Typical meshes present a thick refinement layer next to the boundaries of the optimal designs, while a variable size mesh is generated within the bulk, depending on the the strain energy density. A suitable coarsening step (implemented in the module `COARSEN`) is performed in "void" zones, which are poor in topology and mechanical information. The `ATOPT` algorithm is able to find the main layout of the optimal design in the very first optimization loops, while finer discretizations are conceived to improve the accuracy of the final optimal design. This allows to achieve the same results of large scale optimization approaches, but with a remarkable reduction in terms of computational cost.

The outline of the paper is as follows. Section 2 reports fundamentals of the volume-constrained minimum compliance problem, recalling both the continuous and the discrete formulation herein implemented. Section 3 presents `ATOPT` algorithm, paying peculiar attention to the definition of suitable error estimators and to the progression of refinement and coarsening actions. Section 4 assesses the proposed approach presenting a few numerical simulations, whose features and results are also compared with relevant fixed–grid standard algorithms. Section 5 concludes the paper and points out the main directions of the ongoing research.

2 The Problem

Topology optimization for the maximization of the structural stiffness is herein addressed, according to the well–known *minimum compliance* formulation. The problem of distributing a given amount of linear elastic isotropic material is solved, such that the work of the external load against the corresponding displacement at equilibrium is minimized.
Let $\Omega \subset \mathbb{R}^2$ be a open, bounded domain of $\mathbb{R}^2$ with Lipschitz boundary $\Gamma = \partial\Omega$. Let $\psi \in L^\infty(\Omega)$, with $0 < \underline{\psi} \leq \psi(x) \leq 1$ a.e. in Ω, be a bounded function representing the material density in Ω, where $\underline{\psi} << 1$ is some positive lower bound that is already introduced to avoid any singularity in the analysis of the further derived discrete problem. Let $\mathbf{C} = \mathbf{C}(\psi(x))$ be a fourth order elasticity tensor depending on the material density at the point $x \in \Omega$. According to the well–known SIMP model, see e.g. [5], we assume

$$\mathbf{C}(\psi(x)) = \psi(x)^p \mathbf{C}_0 \quad p > 1 \ ,$$

being $\mathbf{C}_0$ the stiffness tensor for the given isotropic medium and p a penalization parameter that is usually assumed to be equal to 3, see [7].
Let $\mathbf{u}_d$ and $\mathbf{f}_t$ denote the displacement and traction prescribed on $\Gamma_d \subset \Gamma$ and $\Gamma_t = \Gamma \backslash \bar{\Gamma}_d$, respectively.
For a given density material distribution ψ, the displacement field $\mathbf{u}$ solves the following state problem

$$\begin{aligned} \text{div } \sigma &= \mathbf{g} \qquad \text{in } \Omega && (2.1)\\ \sigma &= \mathbf{C}(\psi)\epsilon(\mathbf{u}) && (2.2)\\ \mathbf{u} &= \mathbf{u}_d \qquad \text{on } \Gamma_d && (2.3)\\ \sigma \cdot \underline{\mathbf{n}} &= \mathbf{f}_t \qquad \text{on } \Gamma_t, && (2.4) \end{aligned}$$

where $\epsilon(\mathbf{u}) = \frac{1}{2}\left(\nabla\ \mathbf{u} + \nabla^t \mathbf{u}\right) \equiv \nabla^s \mathbf{u}$.

According to a frequent assumption in topology optimization, no body load will be considered in the sequel, meaning that $\mathbf{g} = \mathbf{0}$.

Let us introduce the following semi-linear form

$$\begin{aligned} &a(\psi; \cdot, \cdot) : L^\infty(\Omega) \times [H^1(\Omega)]^2 \times [H^1(\Omega)]^2 \to \mathbb{R},\\ &a(\psi; \mathbf{u}, \mathbf{v}) := \int_\Omega \mathbf{C}(\psi)\epsilon(\mathbf{u}) : \epsilon(\mathbf{v})\ dx \end{aligned}$$

and the linear functional:

$$\begin{aligned} &\mathcal{W}(\cdot) : [H^1(\Omega)]^2 \to \mathbb{R},\\ &\mathcal{W}(\mathbf{v}) = \int_{\Gamma_t} \mathbf{f}_t \cdot \mathbf{v}\ dx. \end{aligned}$$

We introduce the following spaces

$$\begin{aligned} [H^1_{\Gamma_d}(\Omega)]^2 &= \{\mathbf{u} \in [H^1(\Omega)]^2 : \quad \mathbf{u} = \mathbf{0} \text{ on } \Gamma_d\}\\ [H^1_{\Gamma_d}(\Omega)]^2 \oplus \mathbf{u_d} &= \{\mathbf{u} \in [H^1(\Omega)]^2 : \quad \mathbf{u} = \mathbf{u_d} \text{ on } \Gamma_d\}\ . \end{aligned}$$

Then the weak formulation of the problem (2.1)-(2.4) reads as follows: find $\mathbf{u} \in [H^1_{\Gamma_d}(\Omega)]^2 \oplus \mathbf{u_d}$ such that

$$a(\psi; \mathbf{u}, \mathbf{v}) = \mathcal{W}(\mathbf{v}) \tag{2.5}$$

for all $\mathbf{v} \in [H^1_{\Gamma_d}(\Omega)]^2$.

Let $\mathcal{Q}_{ad}$ be the space of admissible controls, i.e. the density material distribution, with

$$\mathcal{Q}_{ad} = \{\psi \in L^\infty(\Omega) : \quad 0 < \underline{\psi} \leq \psi \leq 1 \text{ a.e. in } \Omega\}.$$

According to the Clapeyron theorem, the continuous formulation of the topology optimization problem for minimum compliance may be therefore written as:

$$\begin{cases} \min\limits_{\psi\in\mathcal{Q}_{ad}} & \mathcal{C}(\psi,\mathbf{u}) = \displaystyle\int_{\Gamma_t} \mathbf{f}_t\cdot\mathbf{u}\ dx = \int_\Omega \psi^p \mathbf{C}_0\ \epsilon(\mathbf{u}) : \epsilon(\mathbf{u})\ dx \\ \text{s.t.} & a(\psi;\mathbf{u},\mathbf{v}) = \mathcal{W}(\mathbf{v}) \quad \mathbf{v}\in[H^1_{\Gamma_d}(\Omega)]^2 \\ & \dfrac{1}{V}\displaystyle\int_\Omega \psi dx \ \le V_f, \end{cases} \tag{2.6}$$

being V_f the available amount of material as a fraction of the whole domain $V=\int_\Omega dx$.

Now, we introduce the discrete version of problem (2.6). Let $\mathcal{T}$ be a conforming and shape regular triangulation of Ω and h_T be the diameter of the element $T\in\mathcal{T}$. Let $\mathbb{V}\subset[H^1(\Omega)]^2$ be the space of piecewise continuous linear finite element functions defined on $\mathcal{T}$, i.e.

$$\mathbb{V}=\{\mathbf{V}\in[H^1(\Omega)]^2 : \quad \mathbf{V}\in[C^0(\bar\Omega)]^2 \text{ and } \mathbf{V}_{|T}\in\mathbb{P}^1 \quad \forall T\in\mathcal{T}\},$$

and $\mathbb{Q}_{ad}\subset\mathcal{Q}_{ad}$ be the finite dimensional space of piecewise constant admissible controls

$$\mathbb{Q}_{ad}=\{W\in\mathcal{Q}_{ad} :\ W_{|T}\in\mathbb{P}^0 \quad \forall T\in\mathcal{T}\}.$$

We also define

$$\begin{aligned} \overset{\text{o}}{\mathbb{V}} &= \{\mathbf{V}\in\mathbb{V}^1_{\mathcal{T}} : \quad \mathbf{V}=0 \text{ on } \Gamma_d\} \\ \overset{\text{o}}{\mathbb{V}}\oplus\mathbf{u}_d &= \{\mathbf{V}\in\mathbb{V}^1_{\mathcal{T}} : \quad \mathbf{V}=\mathbf{u}_d \text{ on } \Gamma_d\}\ , \end{aligned}$$

where we assume $\mathbf{u}_d\in\mathbb{V}$. The finite element approximation to the primal problem (2.1)-(2.4) reads as follows: find $\mathbf{U}\in\overset{\text{o}}{\mathbb{V}}\oplus\mathbf{u}_d$ such that

$$a(\psi;\mathbf{U},\mathbf{V})=\mathcal{W}(\mathbf{V}) \tag{2.7}$$

for all $\mathbf{V}\in\overset{\text{o}}{\mathbb{V}}$.

Therefore, the discrete topology optimization problem can be written as follows:

$$\begin{cases} \min\limits_{\Psi\in\mathbb{Q}_{ad}} & \mathcal{C}(\Psi,\mathbf{U}) = \displaystyle\int_\Omega \Psi^p \mathbf{C}_0\ \epsilon(\mathbf{U}) : \epsilon(\mathbf{U})\ dx \\ \text{s.t.} & a(\Psi;\mathbf{U},\mathbf{V}) = \mathcal{W}(\mathbf{V}) \quad \forall\mathbf{V}\in\overset{\text{o}}{\mathbb{V}} \\ & \dfrac{1}{V}\displaystyle\sum_{T\in\mathcal{T}}\int_T \Psi\ dx \le V_f\ . \end{cases} \tag{2.8}$$

According to the above setting, the same triangulation is adopted to solve both the minimization problem and the solution of the elasticity equations, as introduced in Section 1. The coupling of linear shape functions for the finite element analysis along with a piecewise constant density discretization is well–known to induce the arising of the so–called checkerboarded designs, i.e undesired mathematical minima which are not feasible from the physical point of view, see e.g. [14, 19, 28]. Moreover, one has also to take into account that the discrete formulation in Eqn. (2.8) is not free from the arising of mesh–dependent solutions, meaning that finer meshes allow for the achievement of more branched optimal designs with respect to the ones obtained on coarser grids.
To reduce the space of admissible layouts one may resort to the introduction of suitable procedures that effectively control the appearance of fine–scale structures. Among the others, reference is made to the heuristic approach discussed in [34], which has reported successful results not only against mesh dependence, but also preventing checkerboard. A peculiar feature of this method is its straightforward and low–cost implementation within the optimization procedure, as it will be exploited in the module `OPTIMIZE` described in Section 3.2.

3 The adaptive algorithm

3.1 The Module `SOLVE`

Given a triangulation $\mathcal{T}$ and a discrete density function Ψ, we suppose that the module `SOLVE` outputs the exact Galerkin solution to (2.7)

$$[\mathbf{U}] = \texttt{SOLVE}(\mathcal{T}, \Psi) \ ,$$

i.e. $\mathbf{U}$ is computed via exact linear algebra and exact integration.
The module relies on common sparse solvers that cope with the positive definite matrices arising from the adopted displacement–based discretization. Alternatively, one may resort to advanced methods that are especially conceived to improve the numerical solution of (2.7) when embedded within a topology optimization framework, see e.g. [38] and [2].

3.2 The Module `OPTIMIZE`

Given a triangulation $\mathcal{T}$, we assume that `OPTIMIZE` solves the finite dimensional optimization problem (2.8)

$$[\Psi] = \texttt{OPTIMIZE}(\mathcal{T}) \ ,$$

where $\Psi \in \mathbb{Q}_{ad}$ is the optimal discrete distribution of material.
The Methods of Moving Asymptotes (MMA) (see [37]) is the iterative minimizer that is called via the module `OPTIMIZE` within the proposed algorithm. Each sub–step of the generic optimization loop provides an update of the density field that is based on the computation of the objective function $\mathcal{C}$ and its relevant sensitivities for the current density distribution. The above quantities may be easily derived if the displacement field

is known, meaning that the module SOLVE is called at each sub–step of the optimization loop to compute the Galerkin solution to problem (2.7).
The Gateaux derivative of the compliance functional $\mathcal{C}$ with respect to the variation of the density control variable may be easily derived according to the adjoint method, see e.g. [8]. It reads as follows

$$\langle \frac{\partial \mathcal{C}}{\partial \Psi}(\Psi, \mathbf{U}), \delta\Psi \rangle = - \int_\Omega p\Psi^{p-1}\mathbf{C}_0 \ \epsilon(\mathbf{U}) : \epsilon(\mathbf{U}) \ \delta\Psi \ dx \qquad \forall \delta\Psi \in \mathbb{P}^0 \ .$$

For brevity, we set

$$G(T; \mathbf{U}, \Psi) := - \int_T p\Psi^{p-1}\mathbf{C}_0 \ \epsilon(\mathbf{U}) : \epsilon(\mathbf{U}) \ dx.$$

The filtered version of the derivative of the compliance functional is defined according to the following relation, see [34, 31]:

$$\widehat{G}(T; \mathbf{U}, \Psi) = \frac{\displaystyle\sum_{\tilde{T} \in \mathcal{T}} K(T, \tilde{T}) \int_{\tilde{T}} \Psi \ G(\tilde{T}; \mathbf{U}, \Psi) \ dx}{\displaystyle\int_T \Psi \ \sum_{\tilde{T} \in \mathcal{T}} K(T, \tilde{T}) \ dx} \ , \tag{3.1}$$

where $K(T, \tilde{T})$ is a convolution kernel that may be specialized as:

$$K(T, \tilde{T}) = \max(0; r - \mathrm{dist}(\mathrm{T}, \tilde{\mathrm{T}})).$$

The parameter r is the assigned filter radius against numerical instabilities, while $\mathrm{dist}(\mathrm{T}, \tilde{\mathrm{T}})$ defines the distance between the centers of the triangles T and $\tilde{T}$.

3.3 The Module ESTIMATE

Given a triangulation $\mathcal{T}$, a discrete control Ψ together with the corresponding discrete solution $\mathbf{U}$, we suppose that ESTIMATE outputs two sets of error indicators, namely $\mathcal{E}_\mathcal{C} := \{\eta_{\mathcal{C},T}\}_{T \in \mathcal{T}}$ and $\mathcal{E}_\Psi := \{\eta_{\psi,T}\}_{T \in \mathcal{T}}$ to be used to estimate the Compliance Error and the Topological Error, respectively:

$$[\mathcal{E}_\mathcal{C}, \mathcal{E}_\Psi] = \texttt{ESTIMATE}_\mathcal{C}(\mathcal{T}, \Psi, \mathbf{U}).$$

For the sake of clarity, we assume that the Module ESTIMATE is built upon two internal Modules, namely $\texttt{ESTIMATE}_\Psi$ and $\texttt{ESTIMATE}_\mathcal{C}$, which will be described in the next two Sections.

3.4 The Module $\texttt{ESTIMATE}_{\mathcal{C}}$

Given a triangulation $\mathcal{T}$ and a discrete control variable Ψ, we denote by $\mathbf{U}$ the Galerkin approximation to the solution $\mathbf{u} = \mathbf{u}(\Psi)$ of the following continuous problem

$$a(\Psi; \mathbf{u}, \mathbf{v}) = \mathcal{W}(\mathbf{v})$$

for all $\mathbf{v} \in [H^1_{\Gamma_d}(\Omega)]^2$. We assume that $\texttt{ESTIMATE}_{\mathcal{C}}$ outputs the set of indicators $\mathcal{E}_{\mathcal{C}} := \{\eta_{\mathcal{C},T}\}_{T\in\mathcal{T}}$ to estimate the compliance error $|\mathcal{C}(\Psi, \mathbf{U}) - \mathcal{C}(\Psi, \mathbf{u})|$,

$$[\mathcal{E}_{\mathcal{C}}] = \texttt{ESTIMATE}_{\mathcal{C}}(\mathcal{T}, \Psi, \mathbf{U}).$$

This goal can be accomplished by using, for example, the standard tools of the DWR method [4, 3]. In the following, for the ease of the reader, we recall the main steps of the derivation.

Proposition 3.1. *Let* $\mathbf{u}$ *be the solution to the state problem*

$$a(\Psi; \mathbf{u}, \mathbf{v}) = \mathcal{W}(\mathbf{v})$$

for all $v \in [H^1_{\Gamma_d}(\Omega)]^2$*, with material density* $\Psi \in \mathbb{Q}_{ad}$ *and* $\mathbf{U}$ *be the corresponding Galerkin solution, i.e.*

$$a(\Psi; \mathbf{U}, \mathbf{V}) = \mathcal{W}(\mathbf{V})$$

for all $\mathbf{V} \in \overset{\circ}{\mathbb{V}}$*. Then there holds*

$$\mathcal{C}(\Psi, \mathbf{U}) - \mathcal{C}(\Psi, \mathbf{u}) \leq \sum_{T\in\mathcal{T}} \|j(\mathbf{U})\|_{\partial T} \|\mathbf{u} - \mathbf{U}\|_{\partial T} \ ,$$

with

$$j(\mathbf{U})|_e = \begin{cases} \frac{1}{2}[\Psi^p \mathbf{C}_0 \epsilon(\mathbf{U}) \cdot \mathbf{n}] & e \cap \partial\Omega = \emptyset \\ \Psi^p \mathbf{C}_0 \epsilon(\mathbf{U}) \cdot \mathbf{n} - \mathbf{f}_t & e \subset \Gamma_t \\ 0 & \text{otherwise,} \end{cases}$$

and $[\cdot]$ *denoting the jump across the interelement side* e*.*

Proof. By using Galerkin orthogonality and integration by parts we obtain

$$\begin{aligned}
\mathcal{C}(\Psi,\mathbf{u})-\mathcal{C}(\Psi,\mathbf{U}) &= \int_\Omega \Psi^p\mathbf{C}_0\ \epsilon(\mathbf{u}):\epsilon(\mathbf{u}) - \int_\Omega \Psi^p\mathbf{C}_0\ \epsilon(\mathbf{U}):\epsilon(\mathbf{U}) \\
&= \int_{\Gamma_t}\mathbf{f}_t\cdot(\mathbf{u}-\mathbf{U}) = \int_\Omega \Psi^p\mathbf{C}_0\ \epsilon(\mathbf{u}):\epsilon(\mathbf{u}-\mathbf{U}) \\
&= \sum_{T\in\mathcal{T}}\int_T \Psi^p\mathbf{C}_0\ \epsilon(\mathbf{u}-\mathbf{U}):\epsilon(\mathbf{u}-\mathbf{U}) \\
&= -\sum_{T\in\mathcal{T}}\Big\{\int_T \nabla\cdot(\Psi^p\mathbf{C}_0\ \epsilon(\mathbf{u}-\mathbf{U}))\cdot(\mathbf{u}-\mathbf{U}) \\
&\quad + \int_{\partial T}(\Psi^p\mathbf{C}_0\ \epsilon(\mathbf{u}-\mathbf{U})\cdot\mathbf{n})\cdot(\mathbf{u}-\mathbf{U})\Big\} \\
&= \sum_{T\in\mathcal{T}}\int_{\partial T}(\Psi^p\mathbf{C}_0\ \epsilon(\mathbf{u}-\mathbf{U})\cdot\mathbf{n})\cdot(\mathbf{u}-\mathbf{U}) \\
&\le \sum_{T\in\mathcal{T}}\|j(\mathbf{U})\|_{\partial T}\|\mathbf{u}-\mathbf{U}\|_{\partial T}\ ,
\end{aligned}$$

where in the two last steps we used the fact that the function $\mathbf{U}$ is piecewise linear and we employed Cauchy–Schwarz inequality. □

Remark 3.1. *As it stands, the right hand-side of the above estimate is not strictly speaking an a posteriori error indicator, because it involves the (unknown) exact primal solution. Motivated by [4, 3] we use the following heuristic error estimator in the module* `ESTIMATE` *of the adaptive algorithm* `ATOPT`

$$|\mathcal{C}(\Psi,\mathbf{U})-\mathcal{C}(\Psi,\mathbf{u})| \ \simeq\ \sum_T \eta_{\mathcal{C},T} \quad \textit{with} \quad \eta_{\mathcal{C},T} := h_T\|j(\mathbf{U})\|^2_{\partial T},$$

where h_T is the diameter of the triangle T.

In the sequel, we will use the following notation $\eta_{\mathcal{C}} := \sum_T \eta_{\mathcal{C},T}$.

3.5 The Module $\texttt{ESTIMATE}_\Psi$

Given a triangulation $\mathcal{T}$ and a discrete control Ψ, we suppose that $\texttt{ESTIMATE}_\Psi$ outputs a set of heuristic indicators $\mathcal{E}_\Psi := \{\eta_{\Psi,T}\}_{T\in\mathcal{T}}$ to be used to localize the region where the largest variation of density material takes place

$$[\mathcal{E}_\Psi] = \texttt{ESTIMATE}_\Psi(\mathcal{T},\Psi). \tag{3.2}$$

A natural choice for the error indicators $\eta_{\Psi,T}$ is the following

$$\eta_{\Psi,T} := \frac{1}{2}\sum_{e\subset\partial T}[\Psi]^2_e\ h_T^2\ ,$$

being $[\Psi]_e = \Psi_{|T} - \Psi_{|T'}$ the jump of Ψ across the common edge e shared by the triangles T and T'. Clearly, the quantity $\eta_{\Psi,T}$, being different from zero in "void/material" transition regions, is a good heuristic indicator to localize the boundary of the structure.

In the sequel, we will use the following notation $\eta_\Psi := \sum_T \eta_{\Psi,T}$.

3.6 The Module MARK

Given a partition $\mathcal{T}$, two set of error indicators $\mathcal{E}_{ref}$ and $\mathcal{E}_{coars}$ and marking parameters $\Theta^r, \Theta^c \in [0,1]$, with $\Theta^r >> \Theta^c$, we suppose that MARK outputs two sets $\mathcal{M}_r, \mathcal{M}_c \subset \mathcal{T}$ of elements marked for refinement and coarsening, respectively

$$[\mathcal{M}_r, \mathcal{M}_c] = \texttt{MARK}(\mathcal{T}, \mathcal{E}_{ref}, \mathcal{E}_{coars}, \Theta^r, \Theta^c) \ ,$$

by employing the classical Doerfler marking strategy. For the sake of clarity, we assume that the Module MARK is built upon two internal Modules, namely $\texttt{MARK}_{\texttt{ref}}$ and $\texttt{MARK}_{\texttt{coar}}$, which output the set of elements marked for refinement and coarsening, respectively. They will be described in the next two Sections.

3.7 The Module $\texttt{MARK}_{\texttt{ref}}$

Given a partition $\mathcal{T}$, a set of error indicators $\mathcal{E}_{ref} := \{\eta_{ref,T}\}$ and marking parameter $\Theta^r \in [0,1]$ we suppose that $\texttt{MARK}_{\texttt{ref}}$ outputs a set $\mathcal{M}_r \subset \mathcal{T}$ of elements marked for refinement

$$[\mathcal{M}_r] = \texttt{MARK}_{\texttt{ref}}(\mathcal{T}, \mathcal{E}_{ref}, \Theta^r) \ .$$

In particular, the algorithm reads as follows

$\texttt{MARK}_{\texttt{ref}}$

(1) set $\mathcal{M}_r = \emptyset$

(2) while $\left(\Theta^r \sum_{T\in\mathcal{T}} \eta_{ref,T} \geq \sum_{T\in\mathcal{M}_r} \eta_{ref,T} \right)$

let $T_{\max}$ the triangle maximizing $\eta_{ref,T}$ in $\mathcal{T}\backslash\mathcal{M}_r$

set $\mathcal{M}_r = \mathcal{M}_r \cup T_{\max}$

end

3.8 The Module $\texttt{MARK}_{\texttt{coar}}$

Given a partition $\mathcal{T}$, a set of error indicators $\mathcal{E}_{coar} := \{\eta_{coar,T}\}$ and marking parameter $\Theta^c \in [0,1]$ we suppose that $\texttt{MARK}_{\texttt{coar}}$ outputs a set $\mathcal{M}_c \subset \mathcal{T}$ of elements marked for coarsening

$$[\mathcal{M}_c] = \texttt{MARK}_{\texttt{coar}}(\mathcal{T}, \mathcal{E}_{coar}, \Theta^c) \ . \tag{3.3}$$

In particular the algorithm reads as follows

$\texttt{MARK}_{\texttt{coar}}$

(1) `set` $\mathcal{M}_c = \emptyset$

(2) `while` $\big(\ \Theta^c \sum_{T\in\mathcal{T}} \eta_{coar,T} \geq \sum_{T\in\mathcal{M}_c} \eta_{coar,T}\big)$

let $T_{\max}$ the triangle minimizing $\eta_{coar,T}$ in $\mathcal{T}\backslash\mathcal{M}_c$

`set` $\mathcal{M}_c = \mathcal{M}_c \cup T_{\max}$

`end`

3.9 The Modules REFINE and COARSEN

We suppose that a function `REFINE` is at our disposal that implements iterative or recursive bisection such that, given a triangulation $\mathcal{T}$ and a subset $\mathcal{M}_r \subset \mathcal{T}$ of marked elements for refinement

$$\mathcal{T}_* = \texttt{REFINE}(\mathcal{T}, \mathcal{M}_r) \tag{3.4}$$

outputs a triangulation $\mathcal{T}_*$ where at least all elements of $\mathcal{M}_r$ are refined.
Analogously, we assume that a function `COARSEN` is at our disposal such that, given a triangulation $\mathcal{T}$ and a subset $\mathcal{M}_c \subset \mathcal{T}$ of marked elements for coarsening

$$\mathcal{T}_* = \texttt{COARSEN}(\mathcal{T}, \mathcal{M}_r) \tag{3.5}$$

outputs a triangulation $\mathcal{T}_*$ where at least all elements of $\mathcal{M}_c$ are coarsened.

3.10 The Adaptive Topology Optimization (ATOPT) algorithm

We collect the modules described in the previous Sections and we introduce the `ATOPT` algorithm. Recall that $k \geq 1$ stands for the adaptive counter.

ADAPTIVE TOPOLOGY OPTIMIZATION ALGORITHM (ATOPT)

Given the initial triangulation $\mathcal{T}^{(k)}$, and the parameters $\underline{\Theta} := \{\Theta^{r_0}, \Theta^{r_1}, \Theta^{r_2}, \Theta^c\}$ set $k = 0$ and iterate:

(1) $[\Psi^{(k)}] = \texttt{OPTIMIZE}(\mathcal{T}^{(k)})$

(2) $[\mathbf{U}^{(k)}] = \texttt{SOLVE}(\mathcal{T}^{(k)}, \Psi^{(k)})$

(3) $[\mathcal{E}_{\mathcal{C}}^{(k)}, \mathcal{E}_{\Psi}^{(k)}] = \texttt{ESTIMATE}(\mathcal{T}^{(k)}, \Psi^{(k)}, \mathbf{U}^{(k)})$

(4) $[\mathcal{M}_{r_0}^{(k)}] = \texttt{MARK}_{\texttt{ref}}(\mathcal{T}^{(k)}, \mathcal{E}_{\Psi}^{(k)}, \Theta^{r_0})$

(5) $[\mathcal{M}_{r_1}^{(k)}] = \texttt{MARK}_{\texttt{ref}}(\mathcal{T}^{(k)}, \mathcal{E}_{\mathcal{C}}^{(k)}, \Theta^{r_1})$

(6) $[\mathcal{M}_{r_2}^{(k)}] = \texttt{MARK}_{\texttt{ref}}(\mathcal{T}^{(k)}, \mathcal{E}_{\mathcal{C}}^{(k)}, \Theta^{r_2})$

(7) $[\mathcal{T}^{(k+1/2)}] = \texttt{REFINE}(\mathcal{T}^{(k)}, \mathcal{M}_{r_0}^{(k)} \cup \mathcal{M}_{r_1}^{(k)} \cup \mathcal{M}_{r_2}^{(k)})$

(8) $[\mathcal{M}_{c}^{(k+1/2)}] = \texttt{MARK}_{\texttt{coar}}(\mathcal{T}^{(k+1/2)}, \{\Psi_{|T}^{(k+1/2)} - \underline{\psi}\}_{T \in \mathcal{T}^{(k+1/2)}}, \Theta^c)$

(9) $[\mathcal{T}^{(k+1)}] = \texttt{COARSEN}(\mathcal{T}^{(k+1/2)}, \mathcal{M}_{c}^{(k+1/2)})$, $k := k + 1$

Remark 3.2. *The piecewise constant density function $\Psi^{(k+1/2)}$ is obtained by interpolating $\Psi^{(k)}$ on the new triangulation $\mathcal{T}^{(k+1/2)}$*

Remark 3.3. *The module $\texttt{MARK}_{\texttt{coar}}$ aims at marking for coarsening all elements $T \in \mathcal{T}$ corresponding to "void" regions. In particular, this is achieved by means of the particular choice of the error indicators, i.e. $\{\Psi_{|T} - \underline{\psi}\}_T$ and by choosing $\Theta^c = 0$. This allows to collect all elements with density equal to $\underline{\psi}$, the minimum value allowed for material density.*

Remark 3.4. *The module $\texttt{MARK}_{\texttt{ref}}$ collects elements marked for refinement. In particular, the set $\mathcal{M}_{r_1}^{(k)} \cup \mathcal{M}_{r_2}^{(k)}$ is obtained by performing two consecutive marking steps with the same error indicators, but different marking parameters, i.e. Θ^{r_1} and Θ^{r_2}, with $\Theta^{r_1} > \Theta^{r_2}$. This double marking procedure results to be effective in generating meshes that are especially suited to capture any peak of the strain energy density throughout the domain.*

4 Numerical experiments

This section has the aim of assessing the features and the performances of ATOPT algorithm for minimum compliance design. The numerical experiments have been performed

Example	Figure	Elements	$\eta_{\mathcal{C}}$	η_{Ψ}	Cost Index
1	5(1)	4880	$4{,}50 \cdot 10^{-3}$	$6{,}40 \cdot 10^{-3}$	$1{,}23 \cdot 10^{5}$
	5(2)	4096	$8{,}36 \cdot 10^{-3}$	$12{,}13 \cdot 10^{-3}$	$2{,}50 \cdot 10^{5}$
2a	10(1)	6760	$3{,}82 \cdot 10^{-2}$	$1{,}22 \cdot 10^{-2}$	$0{,}93 \cdot 10^{5}$
	10(2)	6144	$4{,}98 \cdot 10^{-2}$	$1{,}94 \cdot 10^{-2}$	$2{,}15 \cdot 10^{5}$
2b	13(1)	12997	$2{,}08 \cdot 10^{-1}$	$2{,}66 \cdot 10^{-2}$	$2{,}18 \cdot 10^{5}$
	13(2)	12288	$2{,}82 \cdot 10^{-1}$	$9{,}19 \cdot 10^{-2}$	$13{,}40 \cdot 10^{5}$
3	15(4)	15667	$1{,}55 \cdot 10^{-1}$	$2{,}76 \cdot 10^{-2}$	$3{,}55 \cdot 10^{5}$
		16384	$2{,}57 \cdot 10^{-1}$	$4{,}44 \cdot 10^{-2}$	$20{,}98 \cdot 10^{5}$

Table 1: Examples 1–3. Comparisons in terms of compliance error estimator $\eta_{\mathcal{C}}$, topological error estimator η_{Ψ} and cost index CI between optimal designs achieved by `ATOPT` procedure (every first row) and standard optimizations performed on uniformly refined grids with a similar number of elements (every second row).

by using Matlab, see also [32], while the processes of mesh refinement and coarsening have been implemented by using AFEM@Matlab package [13]. In the sequel, we consider few relevant examples in order to comment on the layouts achieved by `ATOPT` method and to compare them with well–known optimal topologies that may be derived on uniform grids. The two sets of error estimators introduced in Section 3.3 are herein used to provide information on the quality of the optimal solutions. The first one, i.e. $\{\eta_{\mathcal{C},T}\}_T$, gives a measure of the error in the approximation of the compliance functional, as solved on the final layout. The second one, i.e. $\{\eta_{\Psi,T}\}_T$, measures the topological error and it is strictly related to the amplitude of the gray regions, especially the intermediate regions that divide "void" zones and "full" material in the optimal designs found by filtered approaches. To set up a comparison in terms of the computational cost between `ATOPT` algorithm and a standard non-adaptive scheme, the index introduced in [24] is adopted. It may be defined as:

$$CI = \sum_{k=1}^{N_R} N_k \cdot I_k, \tag{4.1}$$

where N_k is the number of elements involved in the I_k iterations of the optimization loop acting on the k–th adaptive mesh, while N_R is the total number of adopted grids. The above index assumes a linear cost for each MMA–based optimization procedure

with respect to the number of unknowns, i.e. the number of elements, but it does not take into account the time spent to update the mesh according to the adaptive algorithm. However, the enhanced grid structure and the hierarchical update strategies that are both provided by the software package presented in [13] allow for a very efficient handling of the errors estimate and of the re–meshing operations. The cost index CI may be therefore intended as a robust information that combines fundamental issues of a minimization procedure, which are the number of iterations and the number of elements involved in the optimization process. Table 1 collects the above indexes for the simulations presented in the sequel. For each example the quantities $\eta_{\mathcal{C}} = \sum_T \eta_{\mathcal{C},T}$, $\eta_\Psi = \sum_T \eta_{\Psi,T}$ and the cost index CI are computed for the optimal design achieved by the `ATOPT` procedure and for the result of a standard optimization method on a uniformly refined grid with a comparable number of elements, meaning that the latter has $N_R = 1$ in (4.1).
In all the following examples the stopping criteria for the MMA algorithm is based on the control of the maximum variation of the element–wise density unknowns between two subsequent iterations; when it is smaller than a given tolerance ε, the MMA algorithm stops. The value $\varepsilon = 10^{-2}$ is herein adopted both for the minimizations on the adaptive grids and for the single–run procedures on uniform meshes.
Referring to `ATOPT` algorithm, an additional criteria is needed to stop the iterative mesh refinement. To this purpose the following estimator of the global difference between two subsequent optimal designs is introduced:

$$\Delta_k = \sum_{i=1}^{N_k} a_i^k ||\rho_i^k - \rho_i^{k-1}|| \quad / \quad \sum_{i=1}^{N} a_i^k. \tag{4.2}$$

In the above formula a_i^k and ρ_i^k are the area and the optimal density of the i–th triangle in the k–th mesh of N_k elements, respectively. The quantity ρ_i^{k-1} refers to the projection on the current grid of the optimal density found on the previous one. In all the presented simulations the mesh refinement process is stopped whenever Δ_k is smaller than $2 \cdot 10^{-2}$. Alternatively, a stopping criterium based on $\eta_{\mathcal{C}}$, i.e. based on the control of the compliance error, may be employed.
A final remark is needed to define the main parameters driving the refinement procedure, as detailed in Section 3.10. In order to provide a fine refinement of both bulk and boundaries of the topology, we set $\Theta^{r0} = \Theta^{r1} = 0.7$. The value $\Theta^{r2} = 0.15$ is adopted to capture highly stressed regions, while the coarsening step is straightforwardly managed by the choice $\Theta^c = 0$ (see Remark 3.3). As shown in the sequel, the above parameters allow for adaptive meshes that seem well–suited to address all the considered topologies.

4.1 Example 1.

The first example deals with the geometry described in Figure 1. A squared lamina of unitary thickness is acted upon by a uniform shear load in the lower part of its right edge. The deep cantilever is optimized in order to achieve the maximum stiffness for the enforced volume fraction $V_f = 0.6$. Referring to the elastic properties of the virgin

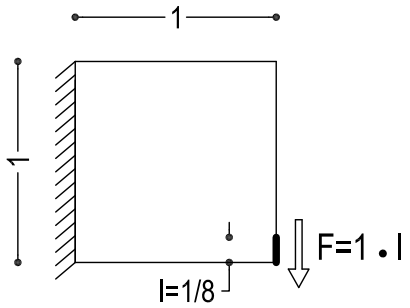

Figure 1: Example 1. Geometrical domain, load and boundary conditions.

material, the Young modulus $E_0 = 1$ is assumed, along with the Poisson ratio $\nu = 0.3$. The minimum dimension of any structural member arising in the optimal design is controlled by the filter radius $r = 1/16$.

Figure 2 shows the optimal designs achieved in the four steps that are needed to find convergence in the implemented procedure. Figure 2(1) refers to the very coarse uniform initial mesh, that is made of 128 triangular elements. In most cases the radius r is shorter than the distance among the centers of the adjacent triangles, meaning that no effective filtering of the sensitivities is applied within this step. The design achieved on the initial mesh sketches the main elements of the topology, i.e. an inclined tie and a low horizontal strut, while checkerboarded patterns arise in the area between the two trusses. The implemented values of Θ^{r0} and Θ^{r1} activate the mesh refinement within the bulk and along the boundaries of the sketched layout. This also provides a finer grid in the central region of the domain, that is affected by the checkerboard phenomenon. The density jump peculiar to checkerboard patterns is in fact straightforwardly detected by the adopted error estimators, thus allowing for a refinement where physical solutions are expected to arise in the case of a richer finite element discretization. Figure 2(2) shows the optimal design achieved on the first adapted mesh made of 438 elements. The diagonal tie and the horizontal struts originally seen in Figure 2(1) are sketched with more accuracy while two thin inclined struts take the place of the checkerboarded patterns found in the previous topology. The optimal design achieved on the second adapted mesh (1722 triangles) is shown in Figure 2(3). This step provides a rough approximation of the expected final layout, with significant topology variations with respect to Figure 2(2). The main diagonal tie is re–shaped in two sub–elements converging on the top of a 45–degrees inclined strut that originates from the lower left corner of the domain. The final result of the adaptive procedure is shown in Figure 2(4) which presents the optimal design achieved on the third adapted mesh involving 4880 triangles. A comparison between Figure 2(3) and Figure 2(4) shows a general improvement in the description of the boundaries of the optimal layout along with a slight modification in the directions of the structural components. This is allowed by the fine discretization at the solid–void interface along with the refinement in the bulk of the design, which is expected to drive the changes in the optimal material distribution. Referring to the features of the two

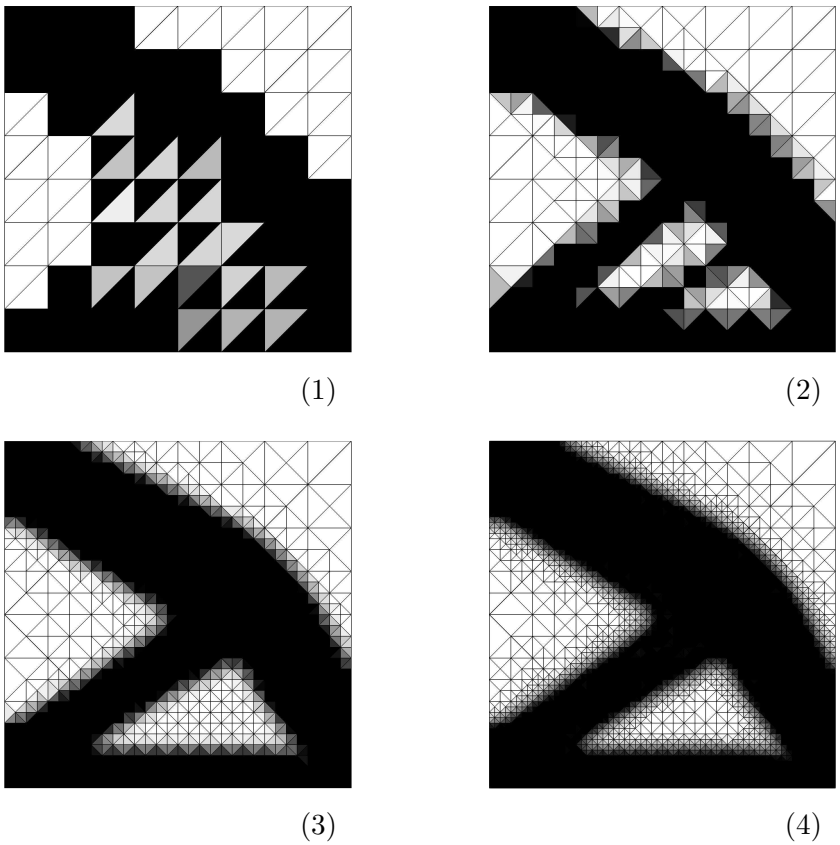

Figure 2: Example 1. Final designs on the meshes generated within the adaptive optimization procedure: steps from 1 to 4.

grids, one may easily notice the effect of the coarsening performed by the last adaptive step in the cavity region, i.e. the "void" area in the lowest part of the domain. This saves a number of elements that were originally introduced to refine a zone of checkerboard instabilities that subsequently evolved in a feasible 0–1 design.
Figure 3 shows the final adapted mesh, i.e. the mesh used to achieve the optimal layout depicted in Figure 2(4). As expected, a nearly uniform grid is found within the bulk of the full material regions, while a fine discretization details the boundary interfaces that are adjacent to coarse "void" zones. Looking at Figure 3, it must be also pointed out that a finer mesh is generated around the load application line and in the vicinity of the ground constraints, i.e. the regions where high strain energy densities are expected. This feature descends from the application of the goal–oriented refinement based on $\eta_{\mathcal{C},T}$ and controlled by the parameter Θ^{r2}.
Figure 4 refers to converge features of `ATOPT` algorithm. Figure 4(L) presents the overall history plot of the compliance functional as recorded throughout the four optimization loops. Black dots stand for the achievement of new computational grids after the use

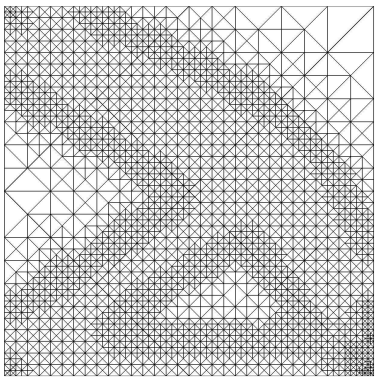

Figure 3: Example 1. Mesh generated in the final step of the adaptive optimization procedure (4880 elements).

of the modules for refinement and coarsening of the mesh. The optimization starts with a uniform distribution of unitary densities all over the coarse mesh made by 128 elements and a very low compliance. The enforcement of the volume constraint calls for a remarkable increase in the objective function during the very first iterations. Afterwards, a smooth convergence is found towards the design presented in Figure 2(1), that is achieved at step 22. The adaptive algorithm refines the mesh and projects the optimal density distribution found for the previous discretization on the new finer grid made of 438 triangles. This induces a local jump in the evaluation of the compliance. The discrete density field achieved by the above mapping becomes the starting point for the second optimization run that calls for 28 iterations in order to provide the optimal design in Figure 2(2). A new adaptive and optimization step lead to the layout in Figure 2(3) after 37 iterations, while the minimization for the achievement of Figure 2(4) is performed in a very few iterations. Looking at Figure 4(L) one may notice that the gap between the compliance value computed at the beginning and at the end of each optimization loop decreases during the process. While the first two refinements are characterized by evolving rough topologies, the last one is only needed to detail an almost stable layout.
Figure 4(R) plots the histories of the error estimator $\eta_{\mathcal{C}} = \sum_T \eta_{\mathcal{C},T}$ for the compliance approximation, and of the global difference Δ_k between two subsequent optimal designs. The above quantities point out that a remarkable improvement is achieved at each iteration both in the strain energy evaluation and in the description of the topology.
Figure 5 presents a final comparison between the optimal design achieved by `ATOPT` procedure on the final grid of 4880 elements and the optimal design found by a standard optimization method working on a uniform mesh of 4096 triangles. The achieved structural layout is approximately the same, but the two discrete solutions are remarkably different with respect to the quality of the designs and the related computational cost.

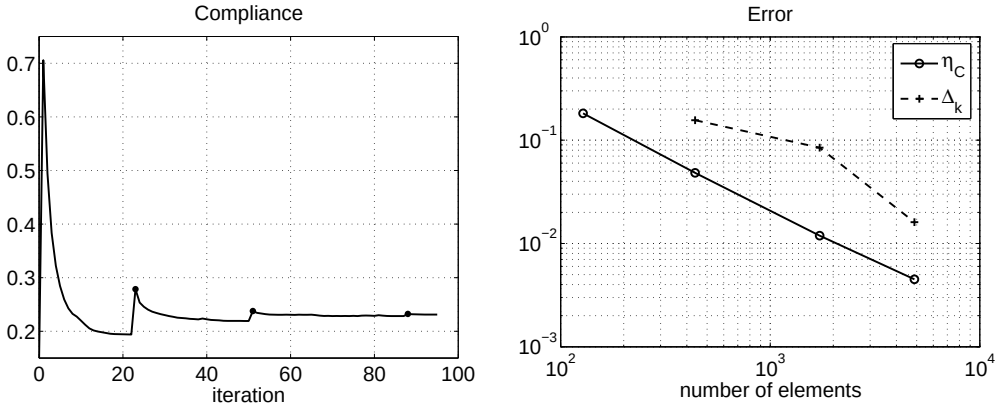

Figure 4: Example 1. History plots for the proposed adaptive optimization procedure: compliance convergence (L) and error evolution (R).

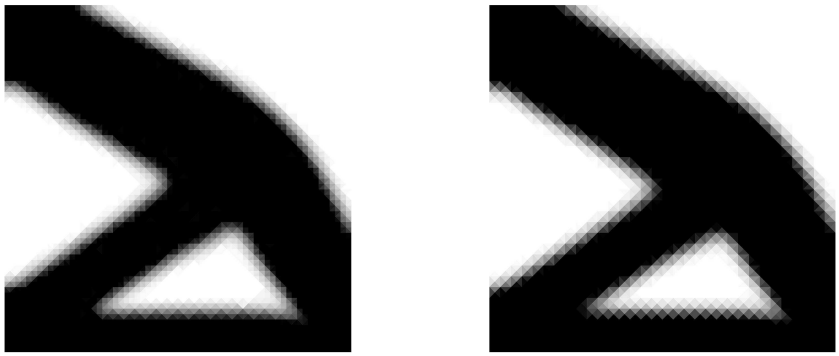

(1) (2)

Figure 5: Example 1. Optimal designs achieved by the proposed procedure on a mesh of 4880 elements (1) and by a standard method on a regular grid of 4096 triangles (2).

A more precise comparison may be performed referring to the first lines of Table 1. They report the compliance error estimator $\eta_{\mathcal{C}} = \sum_T \eta_{\mathcal{C},T}$ for the finite element approximation, the error estimator $\eta_\Psi = \sum_T \eta_{\Psi,T}$ for the topology description and the cost index CI introduced in (4.1). These values are computed on the final design of Figure 5(1) and Figure 5(2), respectively. In Table 1, by looking at the entries referring to Example 1, it may be easily concluded that `ATOPT` algorithm allows for a halving of both the errors and of the computational cost with respect to the standard procedure based on uniformly refined grids. As expected, the adoption of suitable strategies for mesh refinement and coarsening is able to provide a remarkable advantage in the quality of the final designs. Additionally, the very limited number of MMA iterations that are performed on finer adaptive meshes releases the computational burden with respect to procedures that only work on large scale uniform grids.

4.2 Example 2.

The second example refers to the geometry and boundary conditions reported in Figure 6. The rectangular cantilever with ratio 1.5 between the length of the edges is firstly optimized for a volume fraction of $V_f = 0.6$. The elastic property of the material and the filter radius are the same of the previous example. The adaptive procedure needs four optimization loops to meet the enforced requirements on convergence, thus generating the optimal layouts depicted in Figure 7. The first optimal solution is computed on a grid of 192 triangular elements, as presented in Figure 7(1). As before, the adopted filter radius is too short with respect to the coarseness of the starting mesh and the optimizer converges to a minimum that is characterized by an extended checkerboarded region. The marking algorithm easily detects the checkerboarded patterns and provides a suitable refinement, so that the expected bracing structure is found by a new iteration loop on a mesh of 716 elements. Figure 7(2) shows the optimal topology achieved by such a minimization and clearly sketches the optimal layout that will be preserved till the end of the adaptive procedure. The solutions of Figure 7(3) and Figure 7(4) are only needed to improve the quality of the design, while removing unnecessary elements that are located in the "void" regions. They call for 2108 and 6760 triangles, respectively. Figure 8 shows the mesh achieved after the last refinement, that has similar features with respect to the discretization shown in Figure 3. A fine grid is found in the intermediate layer that separates the full material regions from the coarse "void" zones. The bulk of the structure is discretized according to a nearly uniform mesh that is remarkably enriched in the vicinity of the ground constraints, due to the goal–oriented mesh refinement driven by the error indicators $\eta_{\mathcal{C},T}$. The achieved discretization is different with respect to Example 1, where the compactness of the geometrical domain along with the location of the external load remarkably emphasize the role of the loaded region in the evaluation of the overall strain energy.

Convergence features of the proposed example are presented in Figure 9. The compliance history allows to assess the comments made on the evolution of the optimal designs that have been shown in Figure 7. The first two optimization loops are in fact more demanding, in terms of number iterations, with respect to the remaining part of the procedure. The result depicted in Figure 7(2) is found at step 56 over 72, meaning also that less than 30% of the minimization iterations are performed on more than 2000 elements. The design achieved at iteration 56 consists of a rough sketch of the optimal topology that is straightforwardly refined by means of a few additional steps on the last two meshes. Figure 9(R) presents the relevant history plots of the quantities $\eta_{\mathcal{C}}$ and Δ_k. The errors related to the finite element discretization and to the topology description decrease in a substantial way, thus showing the effective role of both criteria in the generation of the adaptive grids.

The optimal design achieved by the proposed procedure on the mesh made of 6760 triangles is finally compared with the result of a standard method performed on a uniform grid of 6144 triangles, see Figure 10. Table 1 provides a direct comparison of the considered error estimators along with the relevant cost indexes, as computed on the final designs. The adaptive procedure allows for a reduction of the error due to the finite

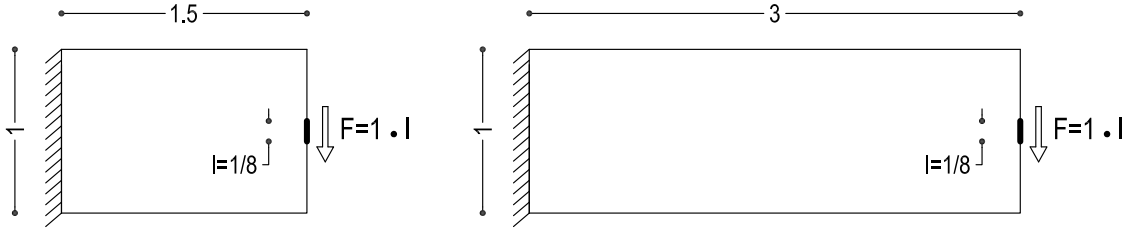

Figure 6: Example 2. Geometrical domain, load and boundary conditions: case a) (L) and case b) (R).

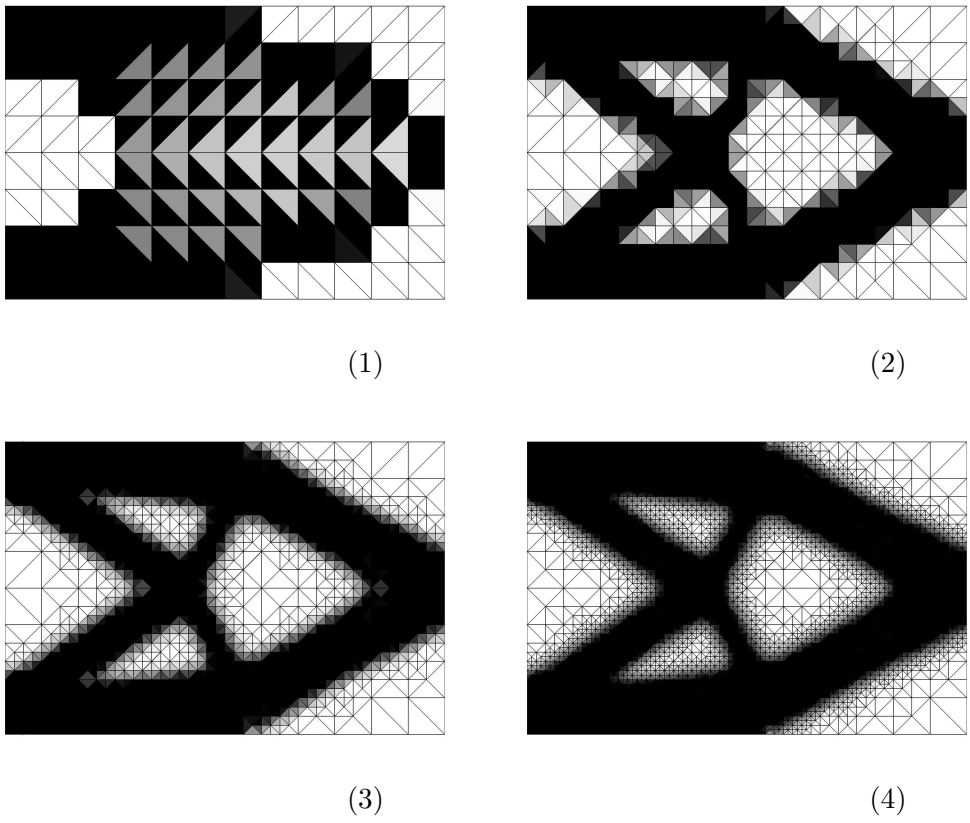

Figure 7: Example 2a. Final designs on the meshes generated within the adaptive optimization procedure: steps from 1 to 4.

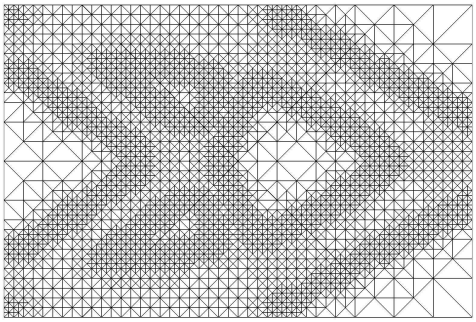

Figure 8: Example 2a. Mesh generated in the final step of the adaptive optimization procedure (6760 elements).

element approximation and of the bias affecting the discrete description of the density field. Such an advantage is achieved with a remarkable computational saving, since the relevant index reports that the cost of the standard procedure is nearly twice as much the burden required by `ATOPT` algorithm. As previously mentioned less than 20 iterations are performed in the adaptive methods on more than 2000 elements, while the uniform grid approach needs approximately 35 iterations on about 6000 triangles.
To investigate the computational features of the proposed adaptive strategy a variation of example 2a is considered. The cantilever in Figure 6(R) is optimized for the volume fraction of $V_f = 0.5$ and a filter radius of $r = 1/16$. The achieved optimal layout is shown in Figure 11, while the mesh adopted in the last optimization loop is depicted in Figure 12. The final grid is made of 12997 triangles and presents many similarities with respect to the mesh of Figure 8. Both the discretizations are characterized by a higher level of refinement around the two regions where the lower strut and the upper tie converge to the ground constraints. Table 1 compares the achieved design with the result of a standard optimization procedure, that is performed on a uniform grid with a similar number of elements, herein 12288. The adaptive procedure allows for a reduction of the compliance error estimator for the finite element approximation $\eta_{\mathcal{C}}$, along with a remarkable improvement of η_{Ψ}. The above result is achieved with a very low computational burden, since the cost index of the fixed–grid procedure is approximately 6 times bigger than the one reported for the adaptive method.
The proposed optimization strategy turns out to be particularly convenient in the case of optimal designs that call for large scale meshes, since it dramatically reduces the number of MMA iterations that are spent on wide sets of unknowns. The `ATOPT` algorithm sketches the main topology on very coarse discretizations, while demanding optimization steps are limited to a few refinements handling the final improvement of the optimal design.

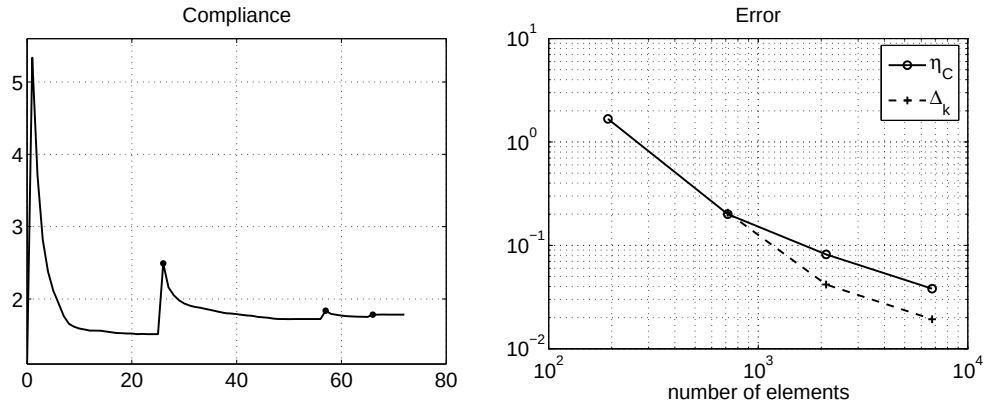

Figure 9: Example 2a. History plots for the proposed adaptive optimization procedure: compliance convergence (L) and error evolution (R).

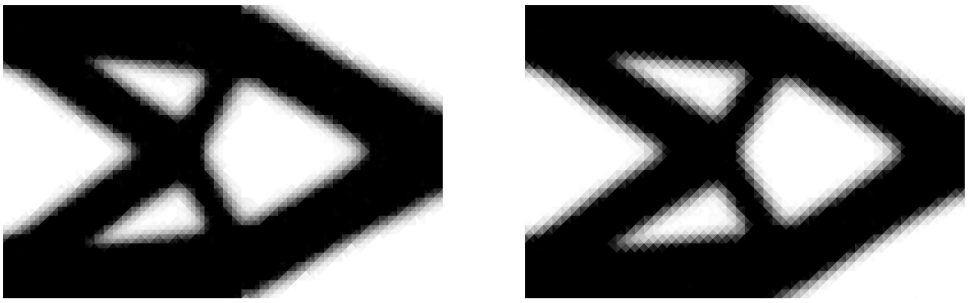

(1) (2)

Figure 10: Example 2a. Optimal designs achieved by the proposed procedure on a mesh of 6760 elements (1) and by a standard method on a regular grid of 6144 triangles (2).

Figure 13 focuses on the same detail of the optimal designs referred in the comparison of Example 2b. The finer discretization of the 0–1 interface that is performed by the the adaptive procedure clearly improves the rendering of the topology solution with respect to the uniform grid of the standard approach. One may also notice the slight variation in the direction of the right side members of the bracing sub–structure in the achieved designs. This is presumably due to the richer discretization of the relevant trusses that is provided by the adaptive mesh in Figure 13(1) with respect to the fixed grid of Figure 13(2).

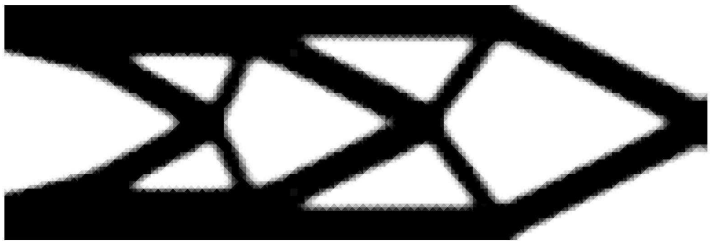

Figure 11: Example 2b. Optimal designs achieved by the proposed procedure on a mesh of 12997 elements.

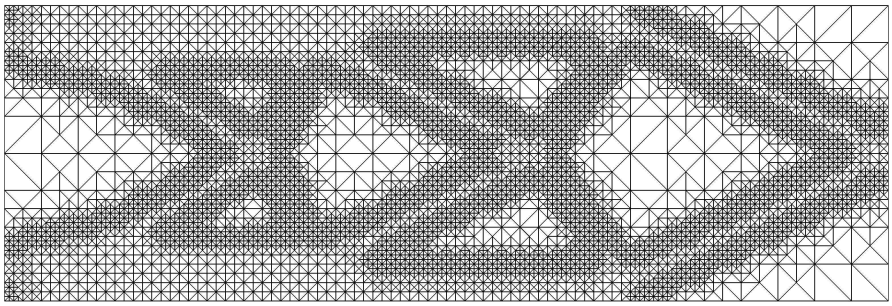

Figure 12: Example 2b. Mesh generated in the final step of the adaptive optimization procedure (12997 elements).

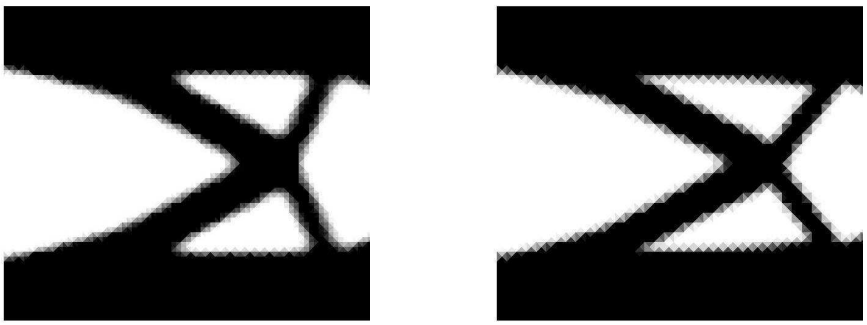

(1) (2)

Figure 13: Example 2b. Details of the optimal designs achieved by the proposed procedure on a mesh of 12997 elements (1) and by a standard method on a regular grid of 12288 triangles (2).

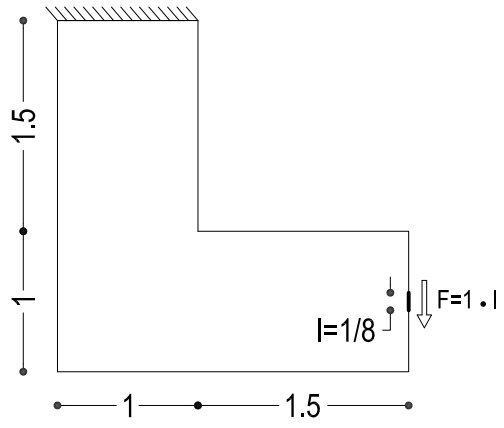

Figure 14: Example 3. Geometrical domain, load and boundary conditions.

4.3 Example 3.

The last example refers to the L–shaped lamina of Figure 14, that is optimized for a volume fraction of $V_f = 0.5$ and a filter radius of 1/16. Elastic properties of the virgin material are those considered in the previous examples. The compliance minimization is accomplished in four optimization loops, achieving the designs presented in Figure 15. In particular, Figure 15(1) shows a coarse mesh of 512 triangles along with the first layout of minimum compliance. The two vertical bars that resist to bending actions are already defined, along with the main elements that make the lower part of the cantilever. The coarseness of the first mesh combined with the adopted measure for the filter radius induces wide checkerboarded areas which are straightforwardly marked for refinement in the subsequent iteration, as found in the previous examples. Figure 15(2) shows the optimal design achieved on the first adaptive grid that involves 1620 elements. The layout defines with more detail the main elements sketched in the previous optimization loop while a set of bars departing from the corner of the geometrical domain is introduced to handle the equilibrium of the compressive trusses in the lower part of the structure. The adaptive procedure provides a fine discretization to each one of the above elements, thus producing a mesh of 5903 triangles. The optimal layout achieved on the new discretization is presented in Figure 15(3). The grid is fine enough to allow for a full action of the enforced filter radius, so that a simplified version of the branched design of Figure 15(2) is found as expected. The discretization in Figure 15(3) clearly shows trails of the older design that mainly consists of very refined zone, but converged to "void". The last update of the mesh allows for a coarsening of these white regions and provides a final refinement to improve the quality of the design. The optimal layout is finally computed on a mesh of 15667 elements, as shown in Figure 15(4).
The evolution of the compliance within the adaptive procedure is presented in Figure 16(L). The plot confirms that the first three optimizations are the more demanding loops in terms of number of iterations. The last minimization takes only a few steps since it only improves the layout description with no remarkable change in the main topology.

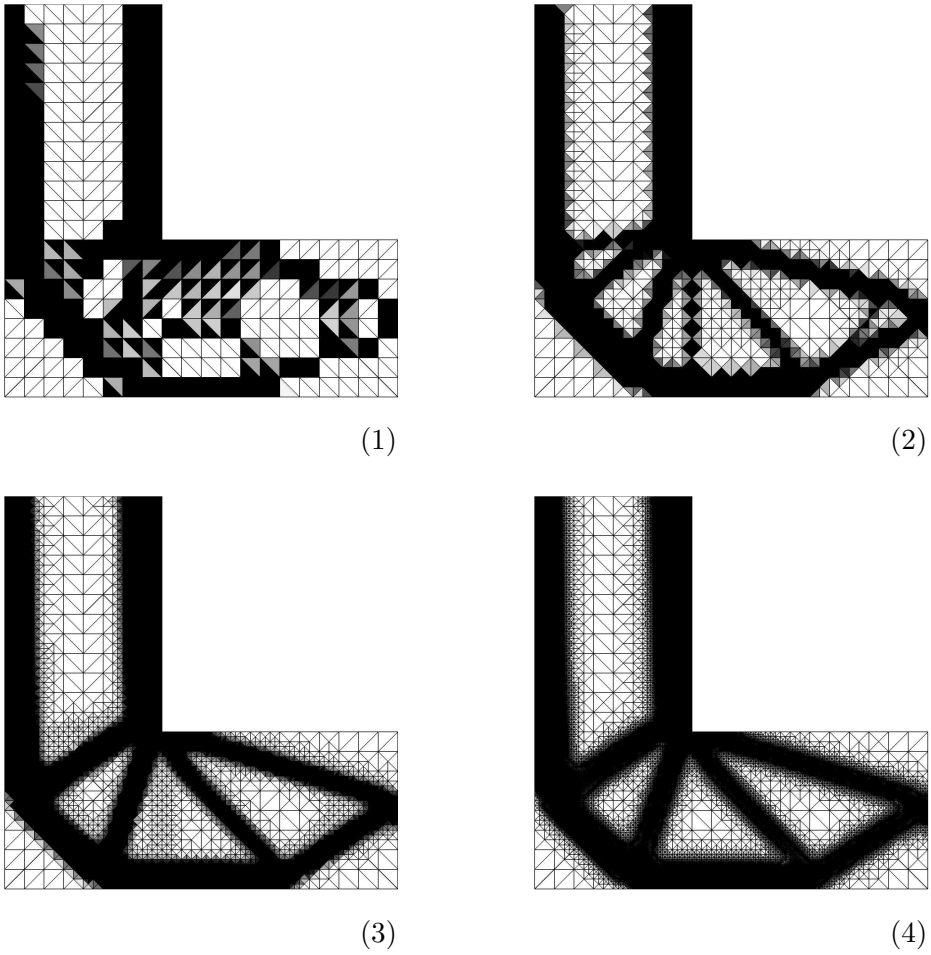

Figure 15: Example 3. Final designs on the meshes generated within the adaptive optimization procedure: steps from 1 to 4.

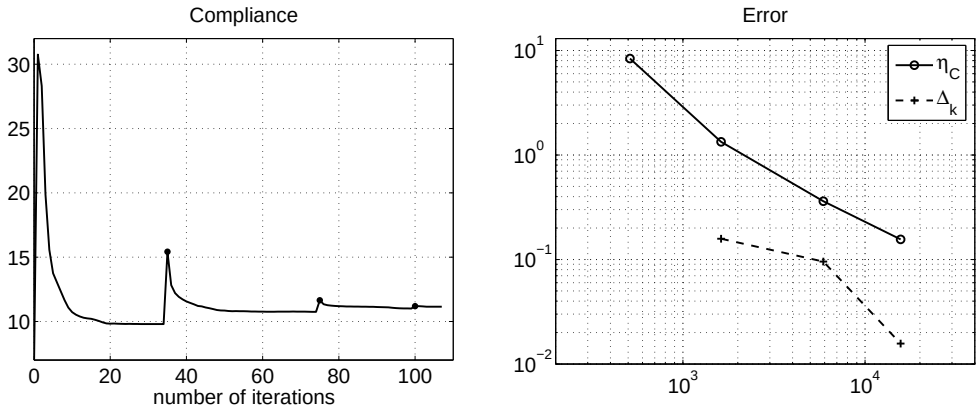

Figure 16: Example 3. History plots for the proposed adaptive optimization procedure: compliance convergence (L) and error evolution (R).

Figure 16(R) presents the history plot of the estimators $\eta_{\mathcal{C}}$ and Δ_k, pointing out the improvements provided by each mesh update. The remarkable peak of the strain energy density that arises in the corner area makes this problem a challenging benchmark to test stress recovery in finite element analysis. Figure 17 shows that the proposed adaptive strategy provides a very fine discretization in such a region. At each update of the mesh the parameter Θ^{r2} controls the additional adaptive refinement based on the error indicators $\eta_{\mathcal{C},T}$. This handles the singularity region and allows to improve the approximation of the global elastic behavior in the evolving optimal topology.
A last remark concerns the comparison of the design achieved by the proposed procedure on the final mesh of 15667 triangles and the optimal layout found by a standard optimization on a uniform grid of about 16000 elements. The last two lines of Table 1 show that the adaptive algorithms allows for a reduction of both error estimates $\eta_{\mathcal{C}}$ and η_{Ψ}. These improvements are achieved with a remarkable saving in terms of computational time. The cost index of the adaptive procedure is nearly 6 times lower than the one found for the uniform grid optimization.

5 Conclusions

We presented an adaptive scheme, named `ATOPT` algorithm, to address volume–constrained compliance minimization. The method is based on the adoption of an iterative procedure that performs a set of optimization loops on a self-adaptive underlying grid. The same mesh is used both for the displacement–based finite element analysis, that exploits low–order triangular elements, and for the discretization of the density field, made through element–wise unknowns. At the end of each minimization loop, two heuristic error estimators are computed in order to evaluate the quality in the description of the topology along with the accuracy of the finite element approximation of the compliance functional. The proposed adaptive strategy, based on the two above error indicators, has

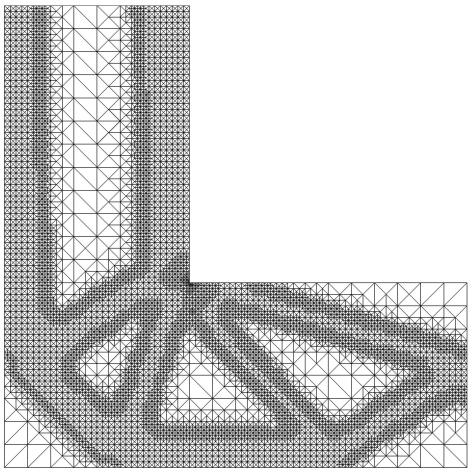

Figure 17: Example 3. Mesh generated in the final step of the adaptive optimization procedure (15667 elements).

the aim of providing a suitable mesh refinement both to the bulk of the optimal design and to the boundaries, while coarsening the "void" regions. An additional refinement step is especially conceived to cope with highly stressed zones, that are captured by the adopted finite element error estimator.
The minimization setting is solved according to a well–known filtered approach that is straightforwardly embedded within the adopted approach to handle the checkerboard problem and to avoid the arising of mesh–dependence in the final layouts. The Method of Moving Asymptotes is iteratively used to address the solution of the optimal problems that are generated within the algorithm. At each update of the mesh the previous optimal solution is projected on the refined discretization as a starting point for the subsequent minimization problem. The optimal layout is therefore gradually achieved through the results found on coarser meshes, while finer discretizations allow to meet the expected accuracy in the description of the design.
Numerical simulations show that the `ATOPT` algorithm is able to find optimal layouts that are in full agreement with standard results based on uniformly refined grids. The achieved meshes are very fine at the boundary of the full material domain and around the regions that are critical for the finite element discretization. Typical zones of major refinement are those next to load application points, ground constraints and geometrical singularities, i.e. where stress and strain peaks are expected to increase the bias in the overall strain energy approximation.
The errors related to the finite element discretization and the topology description are both noticeably lower in the case of the results of the adaptive method with respect to fixed–grid simulations performed on a similar number of elements. Additionally, the

adaptive procedure allows for a remarkable saving in terms of computational cost, if compared to standard methods. Only a few demanding iterations are needed to improve the design approximation on large meshes, since the optimal layout is mainly achieved within the first loops that are performed on a limited number of elements.
The ongoing research is mainly concerned with the extension of the proposed adaptive procedure to alternative formulations and finite element discretizations that are adopted in topology optimization. The accuracy in the handling of energy concentrations and the advantageous computational cost of the proposed method are both features that encourage the application of adaptive algorithms within the framework of stress–based optimization, see e.g. [1, 15, 22]. The same features may be also exploited to improve the effectiveness and the performances of optimization schemes that resort to more demanding finite elements, see e.g. the applications in [9] or [10].

References

[1] Allaire G., Jouve F., Maillot H., Topology optimization for minimum stress design with the homogenization method. *Struct. Multidiscip. Optim.* 2004; **28**,87–98.

[2] Amir O., Stolpe M., Sigmund O. Efficient use of iterative solvers in nested topology optimization. *Struct. Multidisc. Optim.* 2010; 42**1**:55–72.

[3] Bangerth W. and Rannacher R., *Adaptive Finite Element Methods for Differential Equations*, Birkhäuser, 2003.

[4] Becker R. and Rannacher R., An optimal control approach to a posteriori error estimation in finite element methods. *Acta Numer.* 2001; 10:1–102.

[5] Bendsøe M.P. and Kikuchi N., Generating optimal topologies in structural design using a homogeneization method. *Comput. Methods Appl. Mech. Eng.* 1988; **71**(2):197–224.

[6] Bendsøe M.P., Lund E., Olhoff N., Sigmund O., Topology optimization - Broadening the areas of application, *Control and Cybernetics* 2005; **34**(1):7–36.

[7] Bendsøe M.P. and Sigmund O., Material interpolation schemes in topology optimization *Arch. Appl. Mech.* 1999; **69**:635–654.

[8] Bendsøe M.P. and Sigmund O., *Topology optimization - Theory, methods and applications*, Springer, EUA, New York, 2003.

[9] Bruggi M. and Venini P., Eigenvalue-based optimization of incompressible media using mixed finite elements with application to isolation devices *Comput. Methods Appl. Mech. Eng.* 2008;**197**:1262–1279.

[10] Bruggi M. and Venini P., A mixed FEM approach to stress–constrained topology optimization, *International Journal for Numerical Methods in Engineering* 2008; 73: 1693-1714.

[11] Bruyneel M. and Duysinx P., Note on topology optimization of continuum structures includiing self–weight design. *Struct. Multidisc. Optim.* 2005; 29 **4**:245–256.

[12] Bureerat. S. and Limtragool J., Structural topology optimisation using simulated annealing with multiresolution design variables. *Finite Elements in Analysis and Design* 2008; **44**:738–747.

[13] Chen L. and Zhang. C.–S. AFEM@matlab: a Matlab package of adaptive finite element methods. Technique Report, Department of Mathematics, University of Maryland at College Park, 2006.

[14] Diaz A. and Sigmund O., Checkerboard patterns in layout optimization. Struct Multidisc Optim *Multidisc. Optim.* 1995; **19**:89–92.

[15] Duysinx P. and Bendsøe M.P., Topology optimization of continuum structures with local stress constraints. *International Journal for Numerical Methods in Engineering* 1998; **43**:1453–1478.

[16] Fleury C. CONLIN: an efficient dual optimizer based on convex approximation concepts. *Struct Multidiscip Optimization* 1989; 1:81–9.

[17] Guest J.K. and Smith Genut L.C., Reducing dimensionality in topology optimization using adaptive design variable fields. *International Journal for Numerical Methods in Engineering* 2010; **81**(8): 1019–1045.

[18] Jang I.G. and Kwak B.M., Evolutionary topology optimization using design space adjustment based on fixed grid. *International Journal for Numerical Methods in Engineering* 2006; **66**(11): 1817–1840.

[19] Jog C.S. and Haber R.B., Stability of finite element models for distributed–parameter optimization and topology design. *Comput. Methods Appl. Mech. Eng.* 1996; **130**(3–4): 203–226.

[20] Kim I.Y. and Kwak B.M., Design space optimization using a numerical design continuation method. *International Journal for Numerical Methods in Engineering* 2002; **53**(8): 1979–2002.

[21] Kim I.Y. and de Weck O.L., Variable chromosome length genetic algorithm for progressive refinement in topology optimization. *Struct. Multidisc. Optim.* 2005; **29**(6): 445–456.

[22] Le C., Norato J., Bruns T., Ha C. and Tortorelli D., Stress–based topology optimization for continua. *Struct. Multidisc. Optim.* 2010; **41**(4): 605–620.

[23] Lin C.Y., Chou J.N. A two–stage approach for structural topology optimization. *Advances in Engineering Software* 1999; **30**(4):261–271.

[24] Maute K. and Ramm E., Adaptive topology optimization. *Structural Optimization* 1995; **10**(2): 100–112.

[25] Maute K., Schwarz S., Ramm E., Adaptive topology optimization of elastoplastic structures. *Struct. Optim.* 1998; **15**:81–91.

[26] Olhoff N. and Eschenauer H.A., Topology Optimization of Continuum Structures - A Review. *Applied Mechanics Reviews* 2001; **54**:331–390.

[27] Prager W. and Taylor J.E. Problems of optimal structural design. *J. Appl. Mech.* 1968; **35**:102–6.

[28] Rahmatalla S.F. and Swan C.C., A Q4/Q4 continuum structural topology optimization implementation. *Struct. Multidisc. Optim.* 2004; **27**:130–135.

[29] Rannacher R. and Suttmeier F.–T., A feed–back approach to error control in finite element methods: application to linear elasticity. *Computational Mechanics* 1997; **19**:434–446.

[30] Rozvany G.I.N., A critical review of established methods of structural topology optimization *Struct. Multidisc. Optim.* 2009; 37 **3**: 217–237.

[31] Stainko R., An adaptive multilevel approach to the minimal compliance problem. *Communications in Numerical Methods in Engineering* 2006; **22**(2): 109–118.

[32] Sigmund O. A 99 line topology optimization code written in Matlab. *Struct. Multidisc. Optim.* 2001; **21**(2):120–7.

[33] Sigmund O. and Clausen P.M., Topology optimization using a mixed formulation: An alternative way to solve pressure load problems *Comput. Methods Appl. Mech. Eng.* 2007; **196**: 1874–1889.

[34] Sigmund O. and Petersson J., Numerical instabilities in topology optimization: A survey on procedures dealing with checkerboards, mesh-dependencies and local minima. *Struct. Multidisc. Optim.* 1998; **16**(1):68–75.

[35] Stolpe M. and Svanberg K., An alternative interpolation scheme for minimum compliance optimization. *Struct. Multidisc. Optim.* 2001; **22**:116–124.

[36] de Sturler E., Paulino G.H., Wang S., Topology optimization with adaptive mesh refinement. In Proceedings of *The 6th International Conference on Computation of Shell and Spatial Structures IASS-IACM 2008: Spanning Nano to Mega*, Abel JF, Cooke JR (eds). Ithaca, NY, U.S.A., 2008.

[37] Svamberg K., Method of moving asymptotes - A new method for structural optimization. *International Journal for Numerical Methods in Engineering* 1987; **24**(3):359–373.

[38] Wang S., de Sturler E., Paulino G.H., Large–scale topology optimization using preconditioned Krylov subspace methods with recycling. *Int J Numer Meth Eng* 2006; **69**(12): 2441–68.

[39] Yoon G.H., Sndergaard Jensen J., Sigmund O., Topology optimization of acoustic–structure interaction problems using a mixed finite element formulation, *Int. Journ. Numer. Meth. Engin.* 2007; **70**(9):1049–1075.

[40] Zhou M. and Rozvany G.I.N., The COC algorithm, part II: Topological, geometry and generalized shape optimization *Comput. Methods Appl. Mech. Eng.* 1993;**106**:1–26.

MOX Technical Reports, last issues

Dipartimento di Matematica "F. Brioschi",
Politecnico di Milano, Via Bonardi 9 - 20133 Milano (Italy)

27/2010 Matteo Bruggi, Marco Verani:
An adaptive algorithm for topology optimization with goal-oriented error control

26/2010 Francesca Ieva, Anna Maria Paganoni:
Designing and mining a multicenter observational clinical registry concerning patients with Acute Coronary Syndromes

25/2010 G. Pena, C. Prud'homme, Alfio Quarteroni:
High Order Methods for the Approximation of the Incompressible Navier-Stokes Equations in a Moving Domain

24/2010 Lorenzo Tamellini, Luca Formaggia,
Edie Miglio, Anna Scotti:
An Uzawa iterative scheme for the simulation of floating boats

23/2010 Joakim Baeck, Fabio Nobile,
Lorenzo Tamellini, Raul Tempone:
Stochastic Spectral Galerkin and collocation methods for PDEs with random coefficients: a numerical comparison

22/2010 Carlo D'Angelo, Paolo Zunino:
Numerical approximation with Nitsche's coupling of transient Stokes'/Darcy's flow problems applied to hemodynamics

21/2010 Niccolo' Grieco, Francesca Ieva,
Anna Maria paganoni:
Provider Profiling Using Mixed Effects Models on a Case Study concerning STEMI Patients

20/2010 Fabio Nobile, Alfio Quarteroni, Ricardo Ruiz Baier:
Numerical solution of an active strain formulation for the electro-mechanical activity in the heart

19/2010 Loredana Gaudio, Alfio Quarteroni:
hN-adaptive spectral element discretization of optimal control problems for environmental applications

18/2010 Paola F. Antonietti, Nur Aiman Fadel, Marco Verani:
Modelling and numerical simulation of the polymeric extrusion process in textile products